(Received 30 December 2025, Accepted 26 January 2026, Scheduled 11 February 2026)

Lower Cost Variable-Leakage-Flux Reverse-Salient-Pole Permanent Magnet Motor by Reducing Rare-Earth Permanent Magnet Usage

Xiping Liu, Hongzhan Hu, Qianli Jia, Zhangqi Liu*, and Zhiguo Zhu

School of Electrical Engineering and Automation, Jiangxi University of Science and Technology, Ganzhou 341000, Jiangxi, China

ABSTRACT: This paper proposes a novel less-rare-earth variable-leakage-flux reverse-salient-pole motor (LRE-VLF-RSPM). The proposed motor achieves the reverse-salient-pole and variable-leakage-flux characteristics by reasonably arranging three layers of arc-shaped flux barriers between adjacent magnetic poles. Furthermore, it incorporates ferrite magnets to reduce the usage of rare-earth permanent magnets by one-third while maintaining torque output, thereby fulfilling the less-rare-earth objective. First, the paper introduces a rotor topology and operational principle. Subsequently, it employs two-dimensional finite element analysis (FEA) to compare the electromagnetic performance — including torque, flux-weakening capability, constant power speed range (CPSR), and high-efficiency region proportion — among a conventional V-type synchronous motor (CTVSM), a variable-leakage-flux reverse-salient-pole motor (VLF-RSPM), and the LRE-VLF-RSPM. The final results demonstrate that the proposed motor reduces rare-earth usage by one-third compared to the benchmark motor and exhibits superior flux-weakening capability, a wide constant power speed range, and a large high-efficiency region. These findings verify the effectiveness and feasibility of the proposed motor.

1. INTRODUCTION

In response to the call for energy conservation and emissions reduction, the number of pure electric vehicles (EVs) continues to increase, and they have become a major component of new energy vehicles [1, 2]. Due to their advantages in efficiency and power density, permanent magnet synchronous motors (PMSMs) are often adopted as the traction motors in EVs [3, 4]. However, Interior Permanent Magnet Synchronous Motors (IPMSMs) have certain limitations in speed regulation. To increase torque density, a considerable d-axis demagnetizing current is typically required to generate significant reluctance torque, which leads to increased losses and a substantial reduction in efficiency [5, 6].

In recent years, many scholars have proposed various variable-flux motors to meet the multi-operational demands of EVs. Refs. [7–9] propose a hybrid excitation motor. By applying different DC or AC currents to the excitation winding, a wide speed range can be achieved. However, the presence of the excitation winding adds a heat source, imposing certain requirements on thermal management. Motors where the internal magnetic field can be adjusted by changing the magnetization state of low-coercivity (low-Hc) magnets are known as memory motors. Since this type of memory motor uses only a low-Hc permanent magnet, its magnetization state is easily affected by the load current and can undergo uncontrolled changes [10, 11]. Mechanically adjustable flux motors are another feasible approach. These motors use mechanical devices to change the air-gap flux without additional losses, but they rely heavily on moving parts and have a slower response speed than electrical control [12, 13].

The reverse-salient-pole motor is also an important research direction. Its main characteristic is that L_d is greater than L_q. Under low-speed operating conditions, it generates positive reluctance torque through a flux-enhancing effect, improving load capacity. At high speeds, due to its larger d-axis inductance, a smaller d-axis current is sufficient to weaken the main magnetic field, thereby extending the speed range [14, 15]. Refs. [16, 17] propose a variable-leakage-flux permanent magnet synchronous motor (VLF-PMSM). By designing rotor leakage flux bridges and q-axis flux barriers, the saturation level of the leakage flux paths varies between light load and rated load, achieving the purpose of variable air-gap flux. Given the good compatibility between reverse-salient-pole and variable-leakage-flux characteristics, many scholars have combined them to propose variable-leakage-flux reverse-salient-pole motors (VLF-RSPMs) [18]. These motors feature carefully designed flux barriers between adjacent poles, possessing both reverse-salient-pole characteristics and variable leakage flux capability. They offer advantages such as low torque ripple, strong flux-weakening capability, and high efficiency [19–21].

Furthermore, for permanent magnet motors, rare-earth permanent magnet materials are a crucial component, and the price of rare-earth elements has been rising in recent years [22]. Refs. [23, 24] propose a less-rare-earth permanent magnet synchronous motor (LRE-PMSM). This motor aims to reduce the cost of PM machines by minimizing the use of expensive high-

* Corresponding author: Zhangqi Liu (liuzhq@jxust.edu.cn).

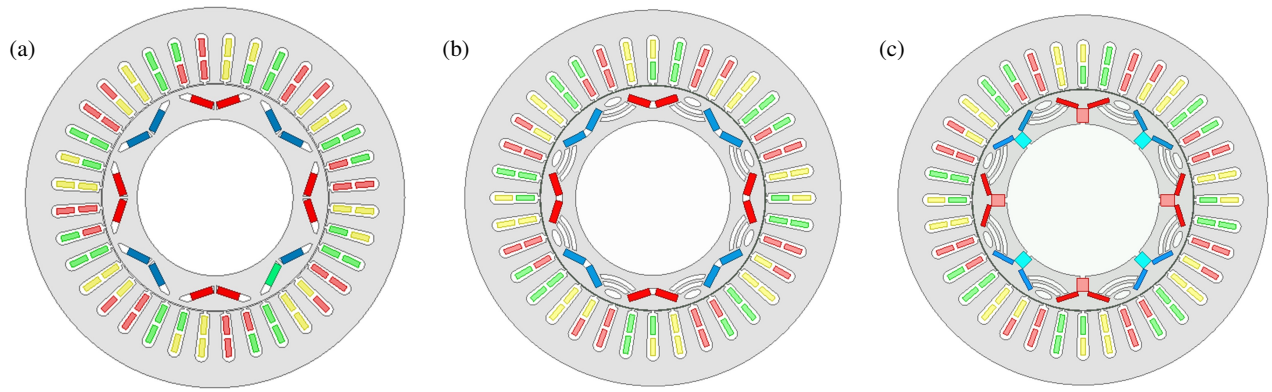

FIGURE 1. Topologies diagram. (a) CTVSM. (b) VLF-RSPM. (c) LRE-VLF-RSPM.

grade rare-earth magnet materials without compromising the associated high performance. The performance degradation caused by the reduced rare-earth magnet content can be compensated by adding low-cost ferrite magnets, achieving significant cost savings through minimizing rare-earth content and enhancing the saliency of the rotor structure.

This paper proposes a less-rare-earth variable-leakage-flux reverse-salient-pole motor (LRE-VLF-RSPM). This motor combines the advantages of the reverse-salient-pole permanent magnet motor (RSPM) and controllable-leakage-flux permanent magnet motor (CLF-PM), realizing both reverse-salient-pole and variable-leakage-flux characteristics through a designed rotor topology. Moreover, by incorporating ferrite magnets to reduce rare-earth usage, it achieves cost savings. The motor is validated and evaluated using the finite element analysis (FEA) method. Calculation results indicate that this motor can broaden the speed regulation capability and maintain nearly unchanged torque output even after a reduction of one-third in rare-earth usage.

2. MOTOR TOPOLOGY AND OPERATING PRINCIPLE

2.1. Motor Topology

This study selects the CTVSM and VLF-RSPM as benchmark motors, both utilizing 100% rare-earth magnets, and further proposes the LRE-VLF-RSPM. The stator structure and winding configuration are identical for all three motor types, featuring a double-layer winding with 8 poles and 36 slots, with the primary distinctions residing in the rotor structures; the topologies are illustrated in Fig. 1. As shown in Fig. 1(a), the CTVSM has its d-axis magnetic circuit formed by V-shaped permanent magnets without a specifically designed q-axis magnetic path, resulting in $L_q > L_d$ which exhibits salient-pole characteristics. Fig. 1(b) illustrates the VLF-RSPM, whose d-axis magnetic circuit also employs V-shaped permanent magnets but incorporates trapezoidal flux barriers between magnets of the same polarity to effectively prevent inter-pole self-leakage flux; additionally, an elliptical flux barrier and two arc-shaped flux barriers are added to the q-axis magnetic path, significantly reducing q-axis inductance to achieve $L_d > L_q$ and thus realize the reverse-salient-pole objective. Simultaneously, these added barriers form two leakage flux paths, achieving the variable-leakage-flux purpose. Fig. 1(c) presents the proposed LRE-VLF-RSPM. Compared to the VLF-RSPM, its q-axis flux barrier design remains unchanged, while in the d-axis circuit, the usage of V-shaped rare-earth permanent magnets is reduced by one-third with a rectangular ferrite magnet added below to compensate for the diminished flux, thereby achieving cost savings. Through this series of evolutionary steps, the final LRE-VLF-RSPM designed in this paper is developed.

2.2. Operating Principle

Compared to CTVSM, VLF-RSPM possesses two distinct characteristics, enabling better flux-weakening speed regulation and offering advantages such as a wider speed range. Building upon this foundation, this paper proposes LRE-VLF-RSPM. To better clarify the distinctions between the motors, the d-q axis magnetic circuits of the three motors are simplified, as shown in Figs. 2(a), (b), and (c). The d-q axis magnetic circuit of the CTVSM is simple, consisting of air gap, stator, rotor cores, and permanent magnets connected in series. In contrast, the VLF-RSPM, due to the added flux barriers in the q-axis, effectively introduces a parallel leakage reluctance in the d-axis and adds a series combination of leakage reluctance and barrier reluctance in the q-axis, achieving the purpose of increasing L_d and decreasing L_q. Compared to the VLF-RSPM, the LRE-VLF-RSPM further reduces rare-earth usage by incorporating a rectangular ferrite block. This is equivalent to adding the magnetomotive force and reluctance of the ferrite block in series within both the d-axis and q-axis magnetic circuits. Consequently, it achieves the goal of reducing rare-earth permanent magnet usage without compromising the reverse-salient-pole and variable-leakage-flux characteristics.

First, the $L_d > L_q$ characteristic is analyzed. Neglecting magnetic saturation effects and angular position, the following expressions can be derived from the given simplified magnetic circuit diagrams:

$$\begin{cases} L_d = \dfrac{N^2}{R_s + R_g + R_\delta || (R_{m1} + R_n + R_r)} \\ L_q = \dfrac{N^2}{R_s + R_g + R_\delta + R_b + R_n + R_r} \end{cases} \tag{1}$$

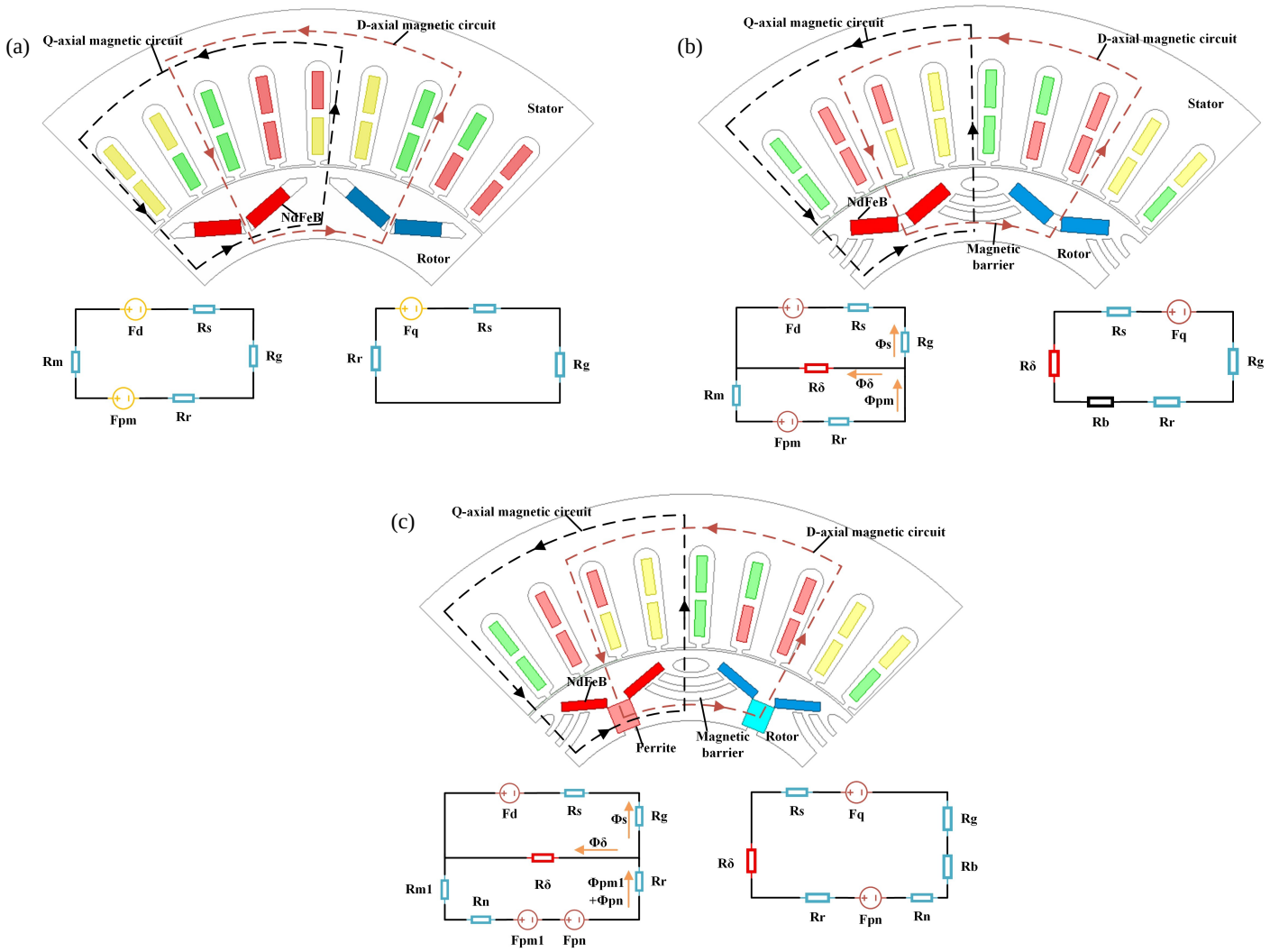

FIGURE 2. Simplified equivalent circuit diagrams of a d-q axis. (a) CTVSM. (b) VLF-RSPM. (c) LRE-VLF-RSPM.

where N is the number of winding turns; R_s, R_g, R_δ, R_{m1}, R_n, R_r, and R_b represent the stator reluctance, air-gap reluctance, leakage-flux-path reluctance, NdFeB magnet reluctance, ferrite magnet reluctance, rotor reluctance, and flux-barrier reluctance, respectively. From Equation (1), it can be seen that the addition of flux barriers in the q-axis achieves $L_d > L_q$, resulting in the reverse-salient-pole characteristic.

Second, the variable-leakage-flux characteristic is analyzed. As shown in Fig. 2(c), the magnetomotive forces (MMFs) of the NdFeB magnet, ferrite magnet, and d-axis are denoted as F_{pm1}, F_{pn} and F_d, respectively; the magnetic fluxes of the NdFeB magnet, ferrite magnet, stator, and leakage flux path are denoted as Φ_{pm1}, Φ_{pn}, Φ_s and Φ_δ, respectively. Thus, the variable-leakage-flux can be expressed as:

$$\begin{bmatrix} \Phi_{pm1}+\Phi_{pn} \\ \Phi_s \end{bmatrix} = \frac{1}{\det R} \begin{bmatrix} R_s+R_g+R_\delta & R_\delta \\ R_\delta & R_r+R_\delta \end{bmatrix} \begin{bmatrix} F_{pm1}+F_{pn} \\ F_d \end{bmatrix} \tag{2}$$

where

$$\begin{aligned} \det R &= \begin{vmatrix} R_s+R_g+R_\delta & R_\delta \\ R_\delta & R_r+R_\delta \end{vmatrix} \\ &= (R_s+R_r)R_r + (R_s+R_g+R_r)R_\delta \qquad (3) \\ \Phi_\delta &= (\Phi_{pm1}+\Phi_{pn}) - \Phi_s \\ &= \frac{(R_s+R_g)(F_{pm1}+F_{pn}) - R_r F_d}{\det R} \qquad (4) \end{aligned}$$

From Formula (3) and Formula (4), it can be concluded that the magnitude of Φ_δ is related to R_s, R_g, R_r, and R_δ. However, when the motor's stator and rotor dimensions are determined, the first three parameters are constant; thus, it can be easily derived that Φ_δ depends on R_δ, where Φ_δ is determined by the dimensions of the leakage flux path. Additionally, it can be inferred that only when $\Phi_\delta \geq 0$, does the motor exhibit the variable-leakage-flux characteristic.

Finally, the less-rare-earth characteristic is analyzed. Specifically, the d-axis magnetic circuit conditions of the LRE-VLF-RSPM and the VLF-RSPM are compared. For the VLF-RSPM,

the magnetomotive force (MMF) and the permanent magnet reluctance are denoted as F_{pm} and R_m, respectively. The permanent magnets in the LRE-VLF-RSPM consist of two parts: NdFeB and ferrite. Consequently, their respective MMFs and reluctances are denoted as F_{pm1}, F_{pn} and R_{m1}, R_n. From the simplified magnetic circuit diagram, it is readily derived that satisfying Equation (5) and Equation (6) achieves the less-rare-earth characteristic.

$$F_{pm} = F_{pm1} + F_{pn} \tag{5}$$

$$R_m = R_{m1} + R_n \tag{6}$$

In summary, this section analyzes the d-q axis inductances, leakage flux, and magnetomotive forces of the proposed LRE-VLF-RSPM, demonstrating the feasibility of achieving the reverse-salient-pole, variable-leakage-flux, and less-rare-earth characteristics, thereby providing sufficient theoretical support for the proposed motor. The key parameters of the CTVSM and the LRE-VLF-RSPM are listed in Table 1. The specific parameters of the VLF-RSPM are identical to those of the CTVSM listed in Table 1.

TABLE 1. Main dimensions and parameters of CTVSM and LRE-VLF-RSPM.

Items	CVTSM	LRE-VLF-RSPM
Rated output power (kW)	6	6
Rated current (A)	28	28
Air-gap length (mm)	0.75	0.75
Rated speed (rpm)	1200	1200
Out diameter of stator (mm)	269.24	269.24
Out diameter of rotor (mm)	110.64	110.64
Numbers of turns	7	7
Slots/Poles	36/8	36/8
NdFeB width/thickness (mm)	16/5	16/3.3
Ferrite PM width/thickness (mm)	/	9.5/8.5
Use of NdFeB per pole/(mm^3)	13331.2	8798.6

3. DESIGN OPTIMIZATION

Based on the aforementioned design and analysis of the LRE-VLF-RSPM, in order to achieve an optimal balance between rare-earth usage and torque output, as well as to optimize performance aspects such as torque ripple and reverse-salience ratio, it is necessary to optimize both its rotor topology and the proportion of the two permanent magnet materials. As shown in Fig. 3, the parametric model of the LRE-VLF-RSPM is presented. Firstly, the required design variables and their variation ranges are determined. Secondly, a sensitivity analysis of these variables is conducted relative to the optimization objectives to identify the primary sensitive variables. Finally, a multi-objective optimization algorithm is applied to the selected sensitive variables to obtain the optimal design scheme.

3.1. Optimization Objectives and Parameter Design

The optimization objectives are defined as follows:

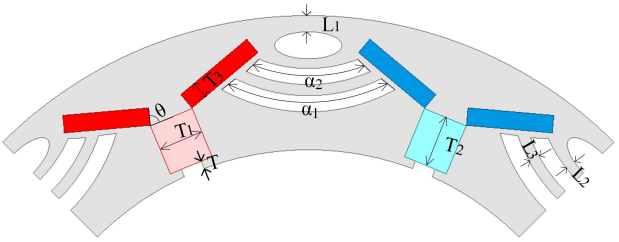

FIGURE 3. Parameterization of the proposed LRE-VLF-RSPM rotor structure.

(1) Maximize the average torque, T_{avg}, under Maximum Torque Per Ampere (MTPA) control.

(2) Minimize the torque ripple, T_{ripple}, which is defined as:

$$T_{ripple} = \frac{T_{\max} - T_{\min}}{T_{avg}} \times 100\% \tag{7}$$

where $T_{\max}$ and $T_{\min}$ are the maximum and minimum torques, respectively.

(3) Maximize the reverse-salience ratio, K_{rs}, which is defined as:

$$K_{rs} = \frac{L_d}{L_q} \tag{8}$$

Based on the parametric model of the LRE-VLF-RSPM presented in Fig. 3, the key parameters are selected as design variables for the subsequent sensitivity analysis. The specific design variables and their variation ranges are listed in Table 2.

TABLE 2. Design variables and variation ranges.

Design variables	Variation Ranges
θ (deg)	[70–80]
T (deg)	[0.5–1.5]
T_1 (mm)	[7.5–10.5]
T_2 (mm)	[9–12]
T_3 (mm)	[3–4]
L_1 (mm)	[1–3]
L_2 (mm)	[1–2]
L_3 (mm)	[1–2]
α_1 (deg)	[35–45]
α_2 (deg)	[45–55]

3.2. Sensitivity Analysis

Given the parametric model of the motor described above, there are numerous variable parameters, and the influence of different variables on the optimization objectives varies significantly. To effectively distinguish the specific degree of impact each variable has on the respective optimization objectives, this paper employs a sensitivity analysis method. The sensitivity index is expressed as:

$$S(x_i) = \frac{D_i}{D} = \frac{V(E(F/x_i))}{V(F)} \tag{9}$$

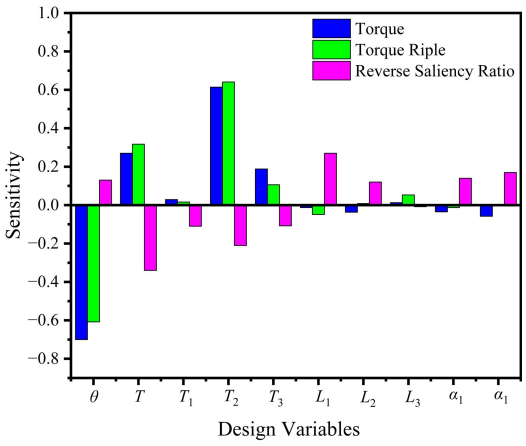

FIGURE 4. Result of sensitivity analysis.

TABLE 3. Optimization results of LRE-VLF-RSPM.

Items	Initial values	Optimized values
θ (deg)	75	72
T (mm)	1	1.2
T_2 (mm)	11	9.5
T_3 (mm)	3	3.3
L_1 (mm)	1.8	2.5
T_{avg} (Nm)	30.4	34.2
T_{ripple} (%)	10.8	8.2
K_{rs}	1.2	1.4

In the equation, x_i represents the input parameter; F denotes the optimization objective function; F/x_i signifies the value of F under the condition where x_i is fixed; E and V represent the expectation and variance of the function, respectively; D_i is the output variance caused solely by the variation of parameter x_i itself; and D is the total variance of the optimization objective function F. The sensitivity indices of each variable relative to the different optimization objectives are shown in Fig. 4. The magnitude of the index value indicates the degree of influence a variable has on an optimization objective, while the sign (positive or negative) indicates whether the correlation between the variable and the objective is positive or negative. As can be seen from the figure, θ has the greatest influence on torque magnitude and shows a negative correlation; T_2 has the greatest influence on torque ripple and shows a positive correlation; T has the greatest influence on the reverse-salience ratio and shows a negative correlation. This demonstrates that the influence of different variables on the various optimization objectives differs significantly and can even be conflicting. Determining the optimal values for each variable cannot be achieved by sensitivity analysis alone; it requires balancing the relationships between the variables and the optimization objectives to obtain the optimal solution.

3.3. Multi-Objective Optimization Based on Key Sensitive Variables

Based on the sensitivity analysis above, the primary sensitive variables are identified as θ, T, T_2, T_3, and L_1, with their variation ranges consistent with those in Table 2. This paper employs Evolutionary Algorithms (EAs) for the multi-objective optimization design, with the specific constraint conditions as follows:

$$T_{avg} \geq 30N; \quad T_{ripple} \leq 12\%; \quad K_{rs} \geq 1.2 \tag{10}$$

The optimization results are presented in Fig. 5, where the optimal operating point is marked. The finally determined optimal values of the key design variables are listed in Table 3.

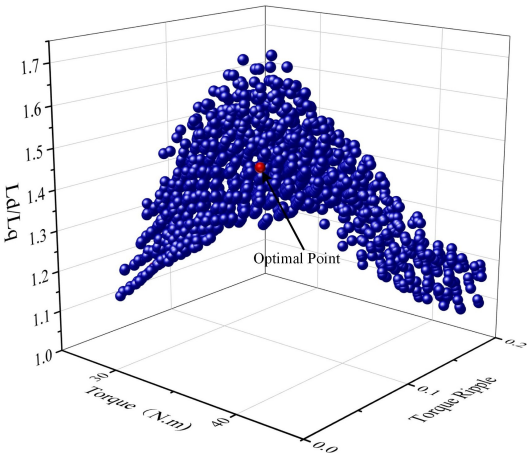

FIGURE 5. Results of optimization.

4. ELECTROMAGNETIC PERFORMANCE ANALYSIS AND COMPARISON

4.1. Magnetic Field Distribution and Variable-Leakage-Flux Characteristics

The flux distributions under no-load conditions for the three motors are shown in Fig. 6. Fig. 6(a) depicts the no-load flux distribution of the CTVSM, where it can be observed that due to the flux barriers at both ends of the magnets, being extremely close to the rotor edge, only a small amount of leakage flux exists. Figs. 6(b) and (c) illustrate the no-load flux distributions of the two variable-leakage-flux motors. As both designs incorporate carefully arranged flux barriers between the magnetic poles, forming two distinct leakage flux paths, a significant amount of leakage flux can be seen flowing along these two paths towards adjacent poles. Fig. 7 presents the flux distributions of the three motors under rated load conditions. From Fig. 7(a), it is evident that the CTVSM still exhibits minor leakage flux under rated load, indicating that its leakage flux shows only a small variation. In contrast, Figs. 7(b) and (c) show that for the two variable-leakage-flux motors, the flux passes through the air gap to the stator side rather than the leakage paths under rated load due to the saturation of the leakage paths, thereby achieving the variable-leakage-flux characteristic.

Furthermore, to better analyze the variable-leakage-flux characteristics of the VLF-RSPM and the LRE-VLF-RSPM, the variation of their d-axis flux linkage with the q-axis armature current is investigated, with the results shown in Fig. 8. When the q-axis armature current is small, the saturation level of the leakage paths is low, resulting in higher leakage flux

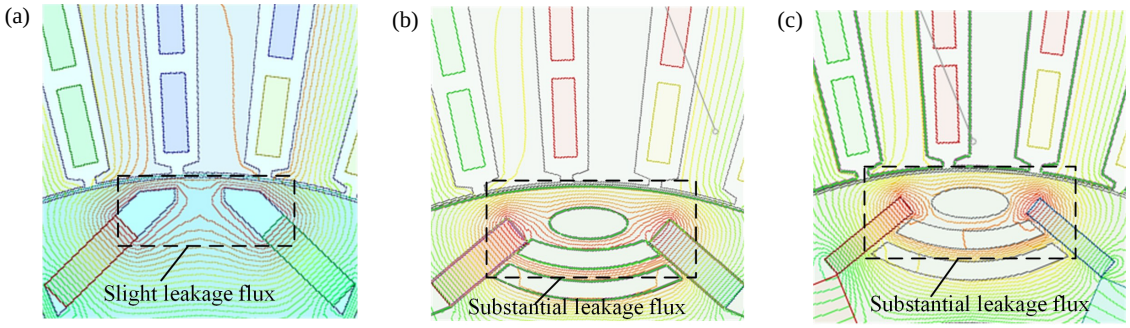

FIGURE 6. Variable flux leakage property of no load. (a) CTVSM. (b) VLF-RSPM. (c) LRE-VLF-RSPM.

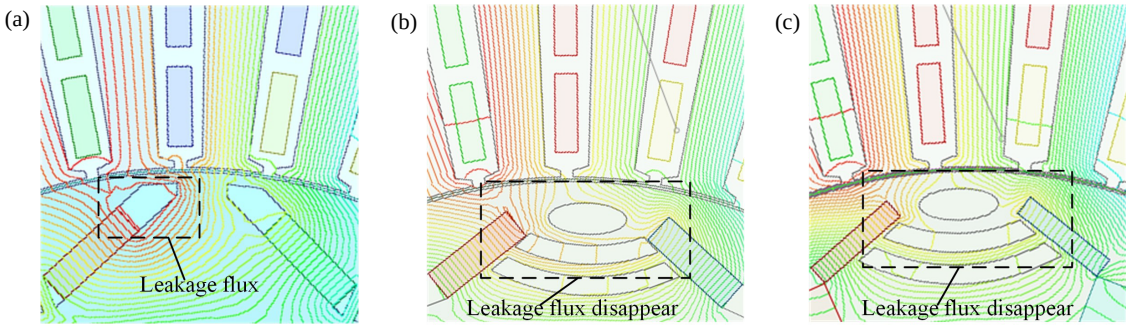

FIGURE 7. Variable flux leakage property of loaded condition. (a) CTVSM. (b) VLF-RSPM. (c) LRE-VLF-RSPM.

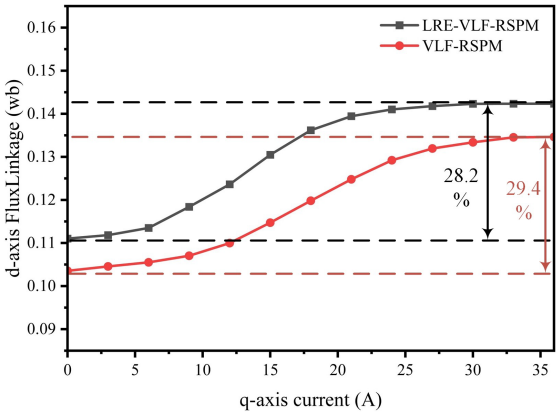

FIGURE 8. Relationship between d-axis flux linkage and q-axis current.

and consequently a smaller d-axis flux linkage. When the q-axis armature current exceeds 28 A, the leakage paths tend to become deeply saturated, with almost no leakage flux, allowing the d-axis flux linkage to reach its maximum. The figure indicates that the variable-flux ranges for the VLF-RSPM and the LRE-VLF-RSPM are 28.2% and 29.4%, respectively.

4.2. No-Load Back-EMF

The no-load back electromotive force (back-EMF) of the three motors is analyzed. Their back-EMF waveforms at the rated speed of 1200 rpm are obtained, with the results shown in Fig. 9. It can be observed that the back-EMFs of the VLF-RSPM and LRE-VLF-RSPM are similar in magnitude, but both are lower than that of the CTVSM. This is because, under no-load conditions, the leakage flux paths in these two motors exhibit a low saturation level, resulting in greater leakage flux and a consequent reduction in the air-gap flux density.

Harmonic analysis of the no-load back-EMF is performed using the Fast Fourier Transform (FFT) method, with the results presented in Fig. 10. The figure indicates that the CTVSM has the highest magnitudes for the 3rd, 5th, 7th, and 9th harmonics. The total harmonic distortion (THD) values of the no-load back-EMF for the CTVSM, VLF-RSPM, and LRE-VLF-RSPM are 12.2%, 8.1%, and 6.6%, respectively. This demonstrates that the no-load back-EMF waveforms of the latter two motors are more sinusoidal.

4.3. Inductance Characteristics

Inductance significantly impacts the motor's output torque and speed regulation range. Therefore, the three motors are investigated under different current conditions, with the results shown in Fig. 11. Fig. 11(a) indicates that the CTVSM consistently maintains $L_q > L_d$, exhibiting salient-pole characteristics. In contrast, Figs. 11(b) and (c) demonstrate that under rated conditions, both the VLF-RSPM and LRE-VLF-RSPM achieve the reverse-salient-pole characteristic of $L_d > L_q$. Furthermore, the rate of decrease in the d-axis inductance is significantly lower than that in the q-axis inductance. It is also evident that compared to the CTVSM, both the VLF-RSPM and the LRE-VLF-RSPM exhibit an increased L_d and a decreased L_q, which aligns with the theoretical analysis presented in Chapter 2. These results confirm the feasibility of the proposed approach of adding flux barriers to achieve the reverse-salient-pole characteristic.

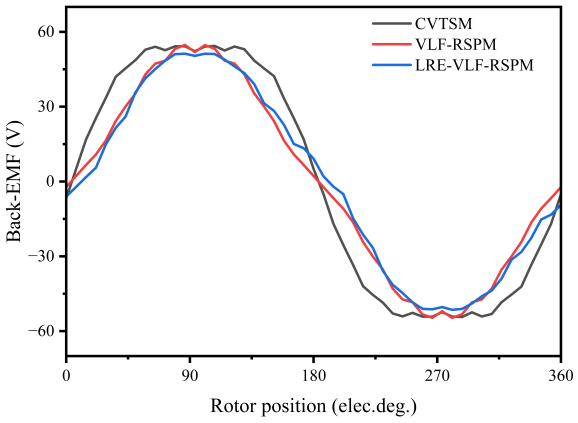

FIGURE 9. Variation of back-EMF with rotor position.

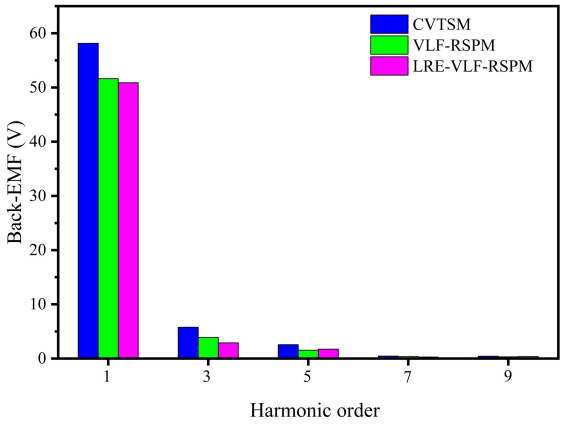

FIGURE 10. Harmonic analysis of the back-EMFs.

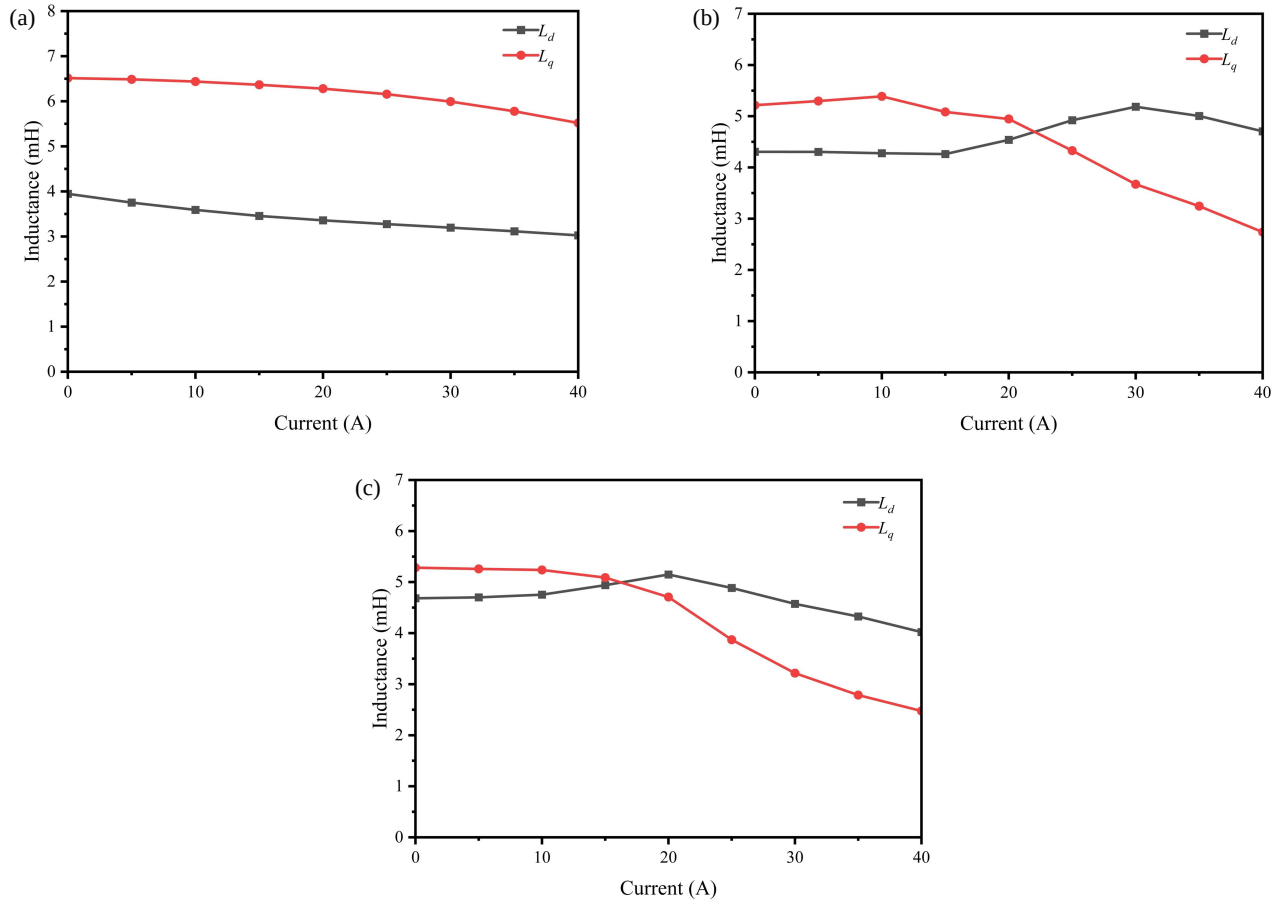

FIGURE 11. Inductance characteristics. (a) CTVSM. (b) VLF-RSPM. (c) LRE-VLF-RSPM.

4.4. Torque Characteristics

Following the analysis of the inductance characteristics in the previous subsection, the torque characteristics are now examined. The electromagnetic torque expression for an Interior Permanent Magnet Synchronous Motor (IPMSM) is given by:

$$T_e = \frac{3P}{2}\left[\Psi_m i_q + (L_d - L_q)\, i_d i_q\right] = \frac{3P}{2}\left[\Psi_m I_s \cos(\beta) + (L_d - L_q)\, I_s^2 \cos(\beta)\sin(-\beta)\right] \quad (11)$$

In the equation, Ψ_m represents the back-EMF linkage of the permanent magnets; I_s is the amplitude of the given current; and β is the given current angle. According to Equation (11), under rated conditions, the CTVSM reaches its maximum torque at a positive current angle, while both the VLF-RSPM and the LRE-VLF-RSPM achieve their maximum torque at a negative current angle, as detailed in Fig. 12. Specifically, the CTVSM attains its peak torque of 40.2 Nm at a current angle of 30°, whereas the VLF-RSPM and LRE-VLF-RSPM reach their peak torques of 35 Nm and 34.2 Nm at current an-

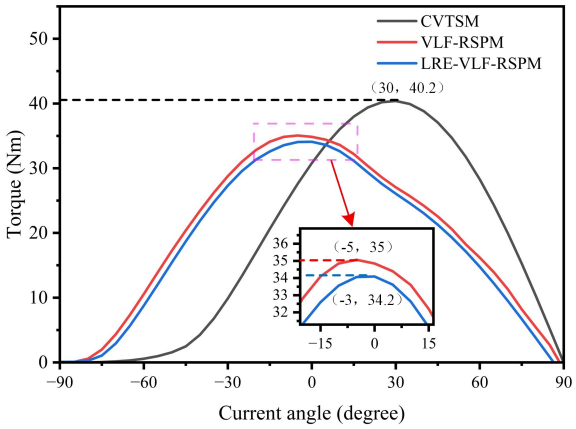

FIGURE 12. Output torque versus current angle.

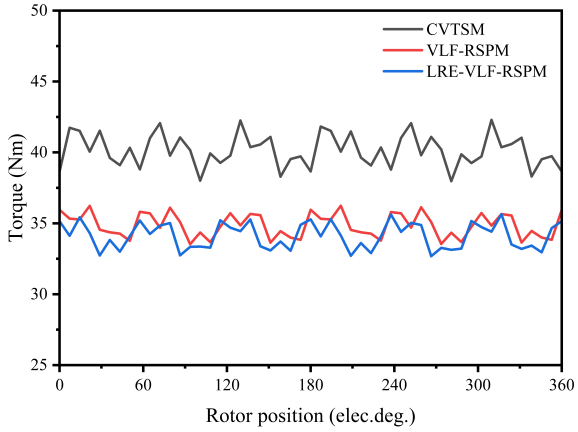

FIGURE 13. Torque ripple.

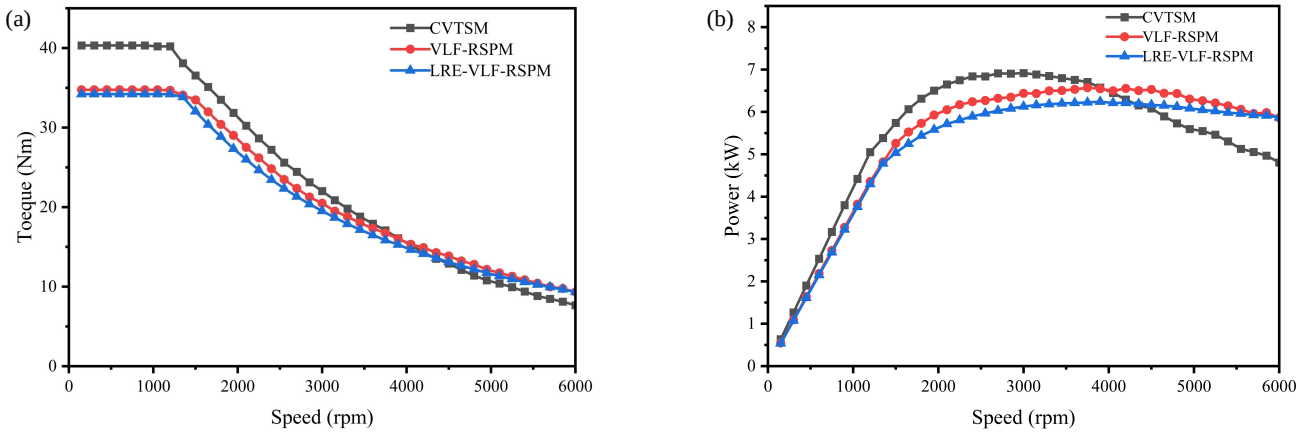

FIGURE 14. (a) Torque-speed. (b) Output power-speed.

gles of $-5°$ and $-3°$, respectively. Furthermore, the figure reveals that even with identical dimensional parameters and rare-earth permanent magnet usage, the torque of the VLF-RSPM is still 12% lower than that of the CTVSM. This reduction is attributed to the reverse-salient-pole characteristic of the VLF-RSPM, which diminishes the reluctance torque. Under the condition of identical dimensional parameters to the VLF-RSPM, the LRE-VLF-RSPM proposed in this paper reduces rare-earth permanent magnet usage by one-third through the addition of ferrite magnets. It can be observed that the output torques of the two motors are fundamentally identical. This demonstrates that the proposed LRE-VLF-RSPM successfully achieves the goal of reducing rare-earth permanent magnet usage.

Figure 13 illustrates the torque ripples of the three motors. It can be observed that the torque ripple of the CTVSM is higher than that of both variable-leakage-flux motors. Specifically, the torque ripple of the CTVSM is 12%, while those of the VLF-RSPM and LRE-VLF-RSPM are 8.6% and 8.2%, respectively. This represents a beneficial outcome of the added flux barriers.

4.5. Torque-Speed and Output Power Characteristics

The flux-weakening capability of a motor determines its speed regulation performance. A wider speed regulation range indicates a stronger flux-weakening capability; therefore, it is essential to investigate the characteristics of torque and output power as functions of speed. Using the Maximum Torque Per Ampere (MTPA) control strategy, the torque-speed and power-speed curves are obtained, as shown in Fig. 14. From Figs. 14(a) and (b), it can be seen that the VLF-RSPM and LRE-VLF-RSPM exhibit identical trends in their respective curves. This once again verifies that the addition of ferrite magnets compensates for the performance deficit caused by the one-third reduction in rare-earth permanent magnets, confirming the feasibility of the less-rare-earth design. Secondly, although the CTVSM exhibits higher torque and power in the low-speed region, its rate of decline is steeper than that of the VLF-RSPM and the LRE-VLF-RSPM. Around 4000 rpm, both its power and torque fall below those of the latter two motors. At 6000 rpm, its power drops to only 4800 W, which is significantly lower than the rated power of 6000 W. These results demonstrate that the VLF-RSPM and LRE-VLF-RSPM possess a wider speed regulation range and stronger flux-weakening capability, which primarily benefits from the reverse-salient-pole characteristic of $L_d > L_q$.

4.6. Core Loss and Efficiency Map

High efficiency is a critical performance indicator for motors, with losses being the primary factor affecting it. Theoretically,

due to the variable-leakage-flux characteristic, the VLF-RSPM and LRE-VLF-RSPM exhibit lower core flux density in the flux-weakening region compared to the CTVSM, resulting in reduced core losses and higher efficiency. The core loss distributions of the three motors at different speeds are shown in Fig. 15. Fig. 15(a) illustrates the core loss distribution of the CTVSM, with a peak loss of 405 W. Figs. 15(b) and (c) show the core loss distributions of the VLF-RSPM and LRE-VLF-RSPM, respectively. It can be observed that their core losses are comparable, with peak losses of 180 W and 225 W, significantly lower than that of the CTVSM. This is attributed to the fact that during flux-weakening operation, the q-axis current is relatively small, keeping the leakage flux paths unsaturated. This condition generates substantial leakage flux, which reduces the core flux and thereby lowers the core loss.

The higher core loss in the CTVSM indicates its correspondingly lower efficiency, as shown in Fig. 16. Comparing Figs. 16(a), (b), and (c), it is evident that the area where

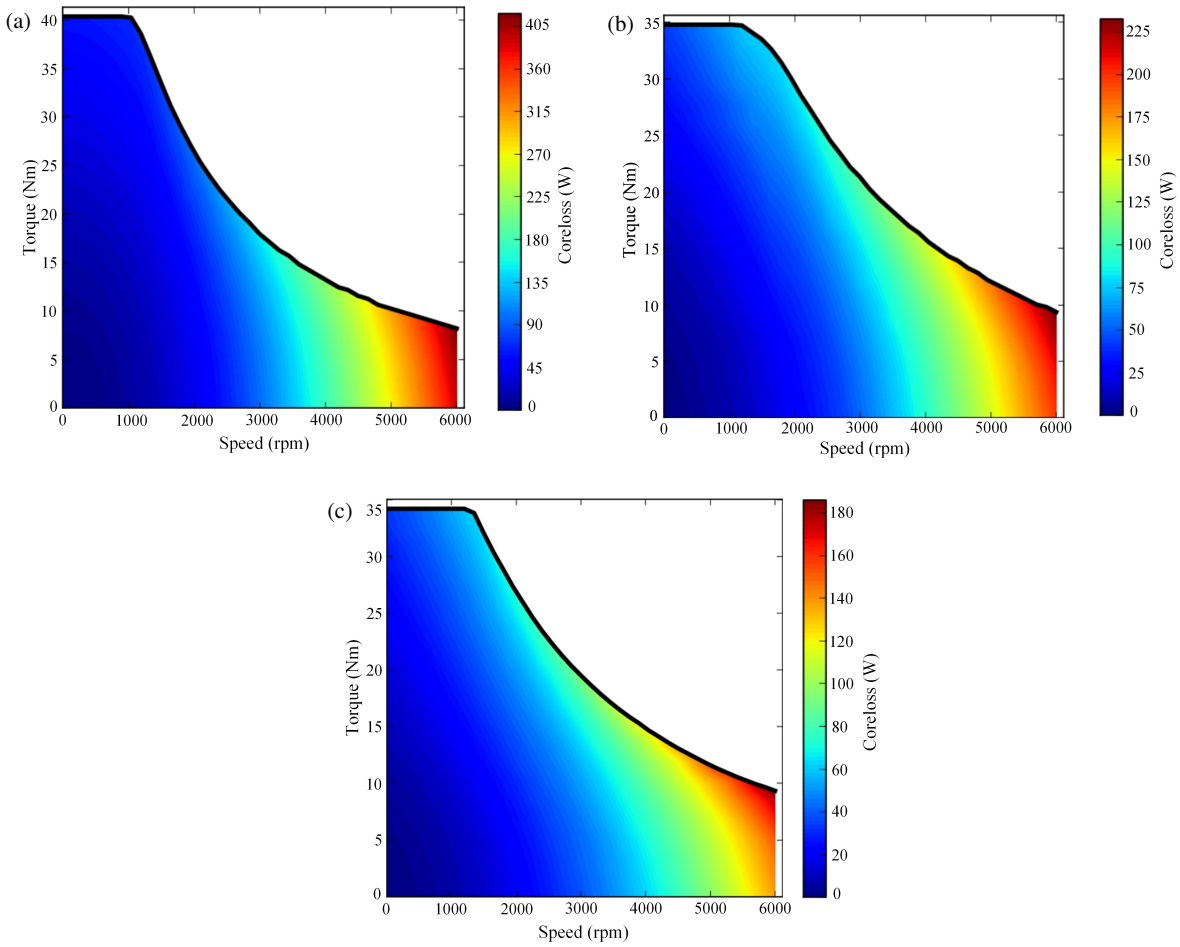

FIGURE 15. Iron loss. (a) CTVSM. (b) VLF-RSPM. (c) LRE-VLF-RSPM.

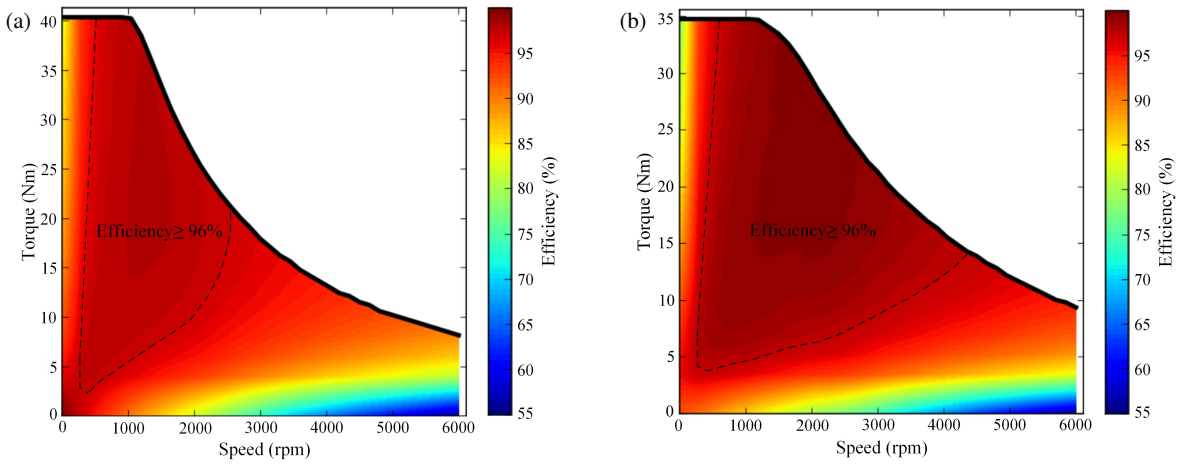

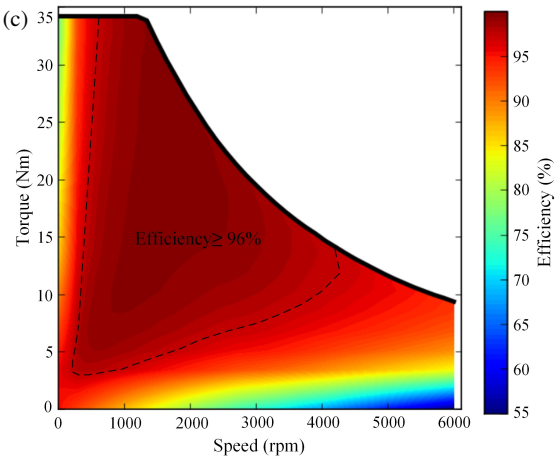

FIGURE 16. The efficiency. (a) CTVSM. (b) VLF-RSPM. (c) LRE-VLF-RSPM.

efficiency exceeds 96% is substantially wider for the VLF-RSPM and LRE-VLF-RSPM than for the CTVSM. These results demonstrate that the VLF-RSPM and LRE-VLF-RSPM offer the advantages of lower losses and a larger high-efficiency region.

5. CONCLUSION

To address the issues that conventional V-type synchronous motors cannot meet the wide speed regulation demands of complex electric vehicle operating conditions and the high cost of rare-earth permanent magnets, this paper, leveraging the advantages of variable-leakage-flux reverse-salient-pole motors, such as a wide speed range and high efficiency, proposes a less-rare-earth variable-leakage-flux reverse-salient-pole motor (LRE-VLF-RSPM). The finite element analysis (FEA) method is employed to evaluate this motor, leading to the following conclusions:

(1) By incorporating ferrite magnets while reducing the usage of rare-earth permanent magnet by one-third compared to the VLF-RSPM, the proposed motor maintains nearly unchanged torque output. It retains the high performance of the VLF-RSPM in terms of variable flux capability, speed regulation, flux-weakening control, and efficiency, thereby achieving the goal of lower cost.

(2) Through rotor structural design, the proposed motor achieves the $L_d > L_q$ characteristic, attains a significant variable-flux range (28.4%), and demonstrates excellent variable-leakage-flux capability. Compared to the CTVSM, it exhibits lower torque ripple, superior flux-weakening capability, and a wider speed regulation range.

(3) Owing to its variable-leakage-flux characteristic, the proposed motor demonstrates lower core loss and a larger high-efficiency region than the CTVSM.

ACKNOWLEDGEMENT

This work was supported in part by the Youth Project of the Natural Science Foundation of Jiangxi Province (20242BAB20219), in part by the Jiangxi Province Early Career Youth Science and Technology Talent Training Project (20244BCE52182), in part by Jiangxi University of Science and Technology High-level Talents Research Special Funds (205200100710), and in part by the Key Program of the Joint Fund of the Natural Science Foundation of Jiangxi Province (20253BAC280024).

REFERENCES

[1] Ehsani, M., K. V. Singh, H. O. Bansal, and R. T. Mehrjardi, "State of the art and trends in electric and hybrid electric vehicles," *Proceedings of the IEEE*, Vol. 109, No. 6, 967–984, Jun. 2021.

[2] Hu, Z., R. T. Mehrjardi, and M. Ehsani, "On the lifetime emissions of conventional, hybrid, plug-in hybrid and electric vehicles," *IEEE Transactions on Industry Applications*, Vol. 60, No. 2, 3502–3511, Mar.-Apr. 2024.

[3] Chen, Z. and G. Li, "A V type permanent magnet motor simulation analysis and prototype test for electric vehicle," *IEEE Access*, Vol. 7, 174 839–174 846, 2019.

[4] Sheela, A. and M. A. Mohan, "Design of permanent magnet synchronous motor for electric vehicle application using finite element analysis," *International Journal of Scientific & Technology Research*, Vol. 9, No. 3, 523–527, 2020.

[5] Wu, W., J. Zhao, R. Zhang, and Y. Dong, "Design and analysis of a new permanent magnet machine with flux-intensifying property," in *2022 IEEE 20th Biennial Conference on Electromagnetic Field Computation (CEFC)*, 1–2, Denver, CO, USA, 2022.

[6] Do, V.-V., T.-A. Huynh, and M.-F. Hsieh, "Design and analysis of flux-intensifying spoke-type IPM motor for improving output torque and flux-weakening performance," in *2022 25th International Conference on Electrical Machines and Systems (ICEMS)*, 1–6, Chiang Mai, Thailand, 2022.

[7] Chu, J., H. Cheng, J. Sun, C. Peng, and Y. Hu, "Multi-objective optimization design of hybrid excitation double stator permanent magnet synchronous machine," *IEEE Transactions on Energy Conversion*, Vol. 38, No. 4, 2364–2375, Dec. 2023.

[8] Wang, X., Y. Fan, Q. Chen, and Z. Wu, "Magnetic circuit feature investigation of a radial-axial brushless hybrid excitation machine for electric vehicles," *IEEE Transactions on Transportation Electrification*, Vol. 9, No. 1, 382–393, Mar. 2023.

[9] Wang, D., D. Zhang, D. Xue, C. Peng, and X. Wang, "A new hybrid excitation permanent magnet machine with an independent AC excitation port," *IEEE Transactions on Industrial Electronics*, Vol. 66, No. 8, 5872–5882, Aug. 2019.

[10] Hu, Y., B. Chen, Y. Xiao, X. Li, Z. Zhang, J. Shi, and L. Li, "Research and design on reducing the difficulty of magnetization of a hybrid permanent magnet memory motor," *IEEE Transactions on Energy Conversion*, Vol. 35, No. 3, 1421–1431, Sep. 2020.

[11] Li, N., D. Xu, X. Hao, and J. Li, "Design and analysis of a series-type permanent magnet axial flux-switching memory machine," *Energies*, Vol. 15, No. 23, 8954, Nov. 2022.

[12] Li, Q., M. Lyu, J. Yang, and S. Huang, "Analysis of a novel mechanically adjusted variable flux permanent magnet homopolar inductor machine with rotating magnetic poles for flywheel energy storage system," *CES Transactions on Electrical Machines and Systems*, Vol. 6, No. 3, 315–323, Sep. 2022.

[13] Sun, T., X. Liu, Y. Zou, C. Huang, and J. Liang, "Design and optimization of a mechanical variable-leakage-flux interior permanent magnet machine with auxiliary rotatable magnetic poles," *CES Transactions on Electrical Machines and Systems*, Vol. 5, No. 1, 21–29, Mar. 2021.

[14] Lu, R., Z. Liu, X. Liu, J. Liang, W. Wu, and W. Wang, "Electromagnetic characteristic analysis and optimization of a novel reverse salient PMSM for wide speed range," *Progress In Electromagnetics Research C*, Vol. 140, 105–115, 2024.

[15] Wang, H., Z. Hao, X. Li, G. Jiang, and L. Guo, "Reverse salient pole design of interior pole-changing permanent magnet synchronous motor," *Journal of Magnetics*, Vol. 29, No. 1, 77–87, 2024.

[16] Yu, X., X. Zhu, L. Quan, Z. Xiang, and D. Fan, "Investigation and regulation of high-efficiency region boundary of variable magnetic flux permanent magnet motor," *Chinese Journal of Electrical Engineering*, Vol. 10, No. 3, 135–146, Sep. 2024.

[17] Xu, L., X. Zhu, W. Wu, W. Fan, X. Zhou, X. Cai, and L. Quan, "Flux-leakage design principle and multiple-operating conditions modeling of flux leakage controllable PM machine considering driving cycles," *IEEE Transactions on Industrial Electronics*, Vol. 69, No. 9, 8862–8874, Sep. 2022.

[18] Liu, X., G. Guo, S. Zhu, and J. Liang, "Design and analysis of variable leakage flux flux-intensifying motor for improve flux-weakening ability," *Progress In Electromagnetics Research M*, Vol. 103, 221–233, 2021.

[19] Liu, X., D. Liu, S. Zhu, and J. Liang, "Investigation of an intensifying-flux variable flux-leakage interior permanent magnet machine for wide speed range," *CES Transactions on Electrical Machines and Systems*, Vol. 6, No. 2, 207–215, Jun. 2022.

[20] Liu, X., S. Zhu, D. Liu, and J. Liang, "Design and analysis of wide speed regulation of variable leakage flux reverse salient-pole motor," *CES Transactions on Electrical Machines and Systems*, Vol. 7, No. 3, 284–293, Sep. 2023.

[21] Du, L., X. Liu, J. Fu, J. Liang, and C. Huang, "Design and optimization of reverse salient permanent magnet synchronous motor based on controllable leakage flux," *CES Transactions on Electrical Machines and Systems*, Vol. 5, No. 2, 163–173, Jun. 2021.

[22] Liu, F., X. Zhu, W. Wu, L. Quan, Z. Xiang, and Y. Hua, "Design and analysis of an interior permanent magnet synchronous machine with multiflux-barriers based on flux-intensifying effect," *IEEE Transactions on Applied Superconductivity*, Vol. 28, No. 3, 1–5, Apr. 2018.

[23] Du, Z. S. and T. A. Lipo, "Cost-effective high torque density bi-magnet machines utilizing rare earth and ferrite permanent magnets," *IEEE Transactions on Energy Conversion*, Vol. 35, No. 3, 1577–1584, Sep. 2020.

[24] Wang, Z., X. Wang, and X. Bao, "A PM dimensions design method for hybrid less rare-earth permanent magnet motors based on analytical approach," *IEEE Transactions on Transportation Electrification*, Vol. 11, No. 2, 6512–6524, Apr. 2025.